Journal of Geochemical Exploration 269 (2025) 107639

Contents lists available at ScienceDirect

Journal of Geochemical Exploration

journal homepage: www.elsevier.com/locate/gexplo

BWM-MARCOS: A new hybrid MCDM approach for mineral potential modelling

Bijan Roshanravan [a], Oliver P. Kreuzer [b,c,*], Amanda Buckingham [d,e]

[a] Department of Mining Engineering, Faculty of Engineering, University of Birjand, Birjand, Iran
[b] Corporate Geoscience Group (CGSG), PO Box 5128, Rockingham Beach, WA 6969, Australia
[c] Economic Geology Research Centre (EGRU), College of Science & Engineering, James Cook University, Townsville, QLD 4811, Australia
[d] Fathom Geophysics Australia, PO Box 1253, Dunsborough, WA 6281, Australia
[e] Centre of Exploration Targeting (CET), The University of Western Australia, 35 Stirling Highway, Crawley, WA 6009, Australia

ARTICLE INFO

Keywords:
Mineral potential modelling
Granites-Tanami Orogen
Gold
BWM
MARCOS

ABSTRACT

Here we describe the application of a novel hybrid multi-criteria decision-making (MCDM) approach termed "Best-Worst-Method-Measurement of Alternatives and Ranking according to COmpromise Solution" (BWM-MARCOS) to mineral potential modelling (MPM). The newly proposed BWM-MARCOS technique combines two mathematical frameworks in which the BWM approach is utilised to weight decision criteria (i.e., predictor maps) whilst the MARCOS approach is applied to rank alternatives. A BWM-MARCOS model of orogenic gold mineral systems in the well-endowed Granites-Tanami Orogen (GTO) in Australia's Northern Territory was generated utilising the same study area and set of competent spatial proxies as previously developed and described by Roshanravan et al. (2020), facilitating the benchmarking of the new results against those obtained from previous models. We found the BWM-MARCOS approach to MPM performed better than any of the knowledge-driven (i.e., fuzzy inference system), continuous (i.e., data-driven index overlay, geometric average and fuzzy gamma) and data-driven (i.e., feed-forward deep neural network and 'original' random forest) mineral prospectivity models previously developed for the GTO by Roshanravan et al. (2020, 2023b). To further constrain the BWM-MARCOS outputs, the modeled gold potential zones were delimited utilising a concentration-area fractal approach. The areas covered by the prioritised 1st order (top priority) and 2nd order (high priority) targets represent significant reductions of the search space (i.e., >303 times or two orders of magnitude, and >93 times or one order of magnitude, respectively). Any order of magnitude, or greater, reduction of the search space, as achieved in this study, can be considered a hallmark of a well-performing, practically useful targeting approach.

1. Introduction

Identifying targets that may contain economically viable mineralisation of the targeted type is a primary goal of mineral exploration. Whilst each type of input data (e.g., remote sensing, geophysics, geology and geochemistry) used in exploration targeting has intrinsic limitations, the combination of such datasets within the framework of mineral potential modelling (MPM) can deliver better outcomes and help to more objectively refine or identify targets for follow-up testing (Kreuzer et al., 2010, 2015, 2019; Ford and Hart, 2013; Lindsay et al., 2016; Nykänen et al., 2017; Roshanravan et al., 2018; Hronsky and Kreuzer, 2019; Yousefi et al., 2019; Parsa et al., 2022; Zuo et al., 2023). Various methods have been developed for MPM that can be broadly categorized into either knowledge- or data-driven techniques (Bonham-Carter, 1994). In the former case, which is typically applied to data-poor greenfields terrains, expert knowledge is utilised to weight and integrate predictor maps given the lack of documented mineral occurrences (Carranza, 2008). Among the different expert-based approaches utilised in knowledge-driven MPM, multi-criteria decision-making (MCDM) methods are highly regarded because of their effectiveness (Bahrami et al., 2019; Karbalaei-Ramezanali et al., 2020; Feizi et al., 2017, 2021; Aryafar and Roshanravan, 2021; Mohammadzadeh et al., 2021; Maghsoudi Moud et al., 2022; Forson and Menyeh, 2023; Riahi et al., 2023a, 2023b).

The ability of MCDM to assess diverse alternatives according to given criteria renders it a highly practical tool for analysing intricate real-

* Corresponding author at: Corporate Geoscience Group, PO Box 5128, Rockingham Beach, WA 6969, Australia.
E-mail address: opkreuzer@gmail.com (O.P. Kreuzer).

https://doi.org/10.1016/j.gexplo.2024.107639
Received 27 June 2024; Received in revised form 28 October 2024; Accepted 13 November 2024
Available online 19 November 2024

world systems, such as mineral systems. The utilization of MCDM techniques in MPM is either comparison-based or matrix-based (Karbalaei-Ramezanali et al., 2020). To allocate weights to individual predictor maps and combine the weighted individual predictor maps into prospectivity maps, the former and latter techniques, respectively, are employed. Although numerous published matrix-based MCDM techniques are available, it is crucial that we keep developing methods with simpler algorithms designed to generate more reliable results and minimize uncertainty caused by incorrect mathematical computations. In this regard, the Measurement of Alternatives and Ranking according to COmpromise Solution (MARCOS) method, comprising seven straightforward stages, has been introduced by Stević et al. (2020). In spite of the technique's robustness and numerous prior applications (e.g., Stević et al., 2020; Celik and Gul, 2021; Deveci et al., 2021; Ecer and Pamucar, 2021; Nguyen et al., 2022; Altay et al., 2023; Zeng et al., 2024), it has been rarely, if ever, used in the context of MPM. Conventional comparison-based MCDM techniques like the analytic hierarchy process (AHP: Saaty, 1980) have drastic obstacles due to the inconsistencies and the substantial number of pairwise comparisons present in these techniques. The Best-Worst Method (BWM: Rezaei, 2015), a novel comparison-based MCDM technique that has been effectively utilised in MPM (e.g., Bahrami et al., 2019; Karbalaei-Ramezanali et al., 2020; Aryafar and Roshanravan, 2021; Feizi et al., 2021; Forson and Menyeh, 2023; Riahi et al., 2023a, 2023b), can decrease the number of required comparisons and yield a higher consistency ratio than similar procedures, enhancing output reliability.

This paper showcases the mechanics and applicability of a novel hybrid MCDM technique termed the "Best-Worst Method-Measurement of Alternatives and Ranking according to COmpromise Solution" (BWM-MARCOS). Combining comparison- and matrix-based methods, namely BMW and MARCOS, the BWM-MARCOS technique was used to identify gold exploration targets in the Granites-Tanami Orogen (GTO), Northern Territory, Australia, which has been subjected to eight prior MPM studies (Roshanravan et al., 2020, 2021, 2023b) and, therefore, provides an excellent opportunity for benchmarking MPM results. More specifically, our newly devised BWM-MARCOS approach to MPM utilised the same study area and set of competent spatial proxies previously described by Roshanravan et al. (2020). By adopting this preconceived framework, we were able to directly compare the new BWM-MARCOS-derived to the previous MPM results reported by Roshanravan et al. (2020, 2021, 2023b), which were obtained using a variety of knowledge-driven (i.e., fuzzy inference system), continuous (i.e., data-driven index overlay, geometric average and fuzzy gamma) and data-driven (i.e., feed-forward deep neural network (FF-DNN), 'original' random forest (RF), cuckoo optimization algorithm in combination with support vector regression (COA-SVR) and 'normalized' RF) approaches.

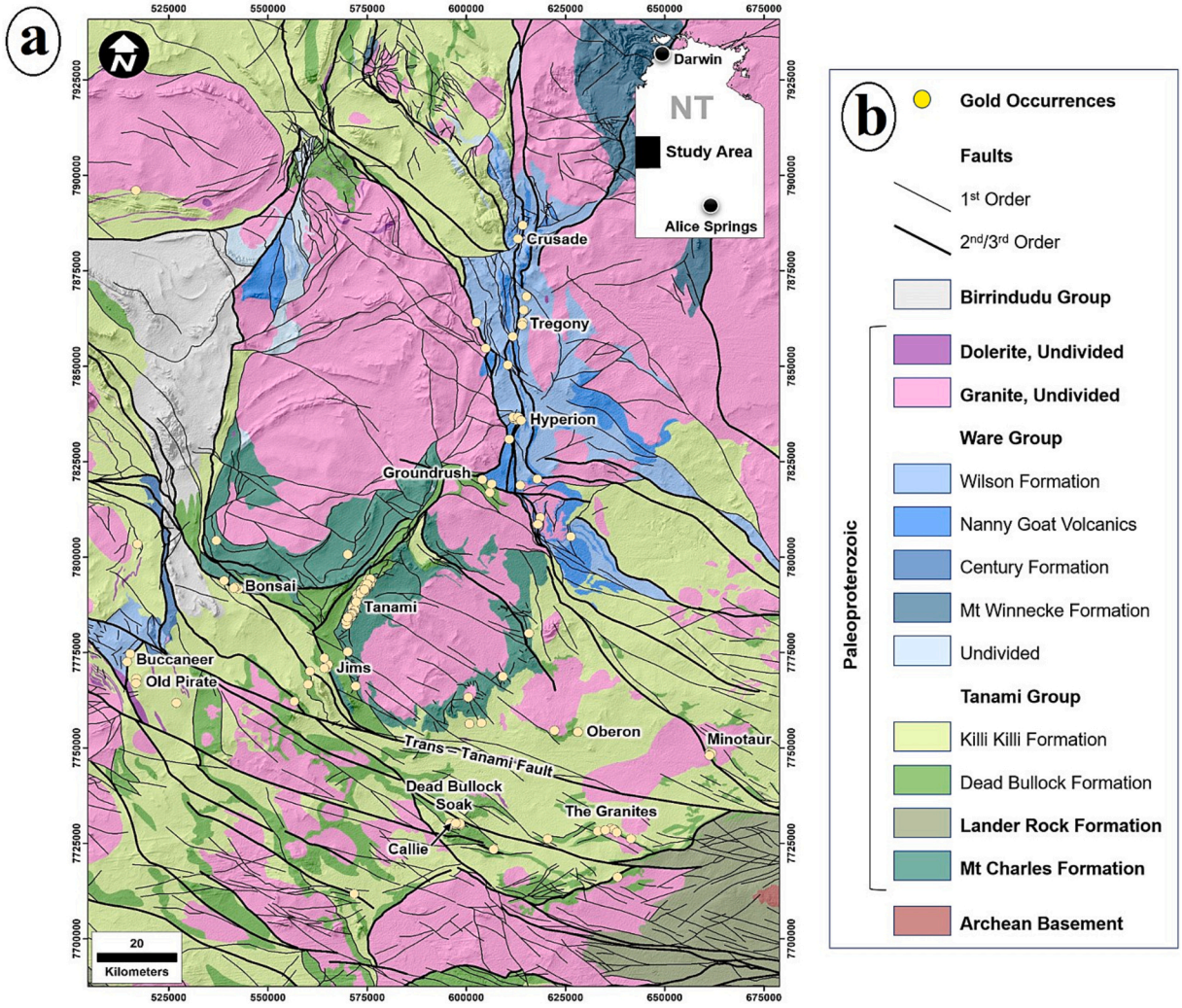

Fig. 1. (a) Solid geology map of the GTO, Northern Territory (modified from Dr. Leon Vandenberg, unpublished data), draped over digital terrain model. Also shown are the main gold occurrences with the key gold camps and deposits labelled. Inset: Location of the study area in the western-central Northern Territory. (b) Map legend.

2. Gold mineralisation in the Granites-Tanami Orogen (GTO)

2.1. Geology and mineralisation

The GTO (Fig. 1), a Neoarchean to Paleoproterozoic tectonostratigraphic element of the largely concealed, southwestern segment of the Precambrian-age North Australian Craton (Kumwenda et al., 2023), is the most significant gold producing belt of Australia's Northern Territory. Much of the sizeable gold endowment of the GTO of >20 million ounces (Crawford et al., 2024) is captured in the Dead Bullock Soak (>14.0 million ounces), Tanami (2.0 million ounces) and Granites (>1.0 million ounces) goldfields as well as the Titania-Oberon (>5 million ounces), Groundrush (1.5 million ounces), Buccaneer (0.6 million ounces) and Coyote-Bald Hill (0.5 million ounces) deposits (Roshanravan et al., 2020; Crawford et al., 2024). Radiometric age dates and structural and geological relationships support a Paleoproterozoic (c. 1795 Ma) age of the gold mineralisation in the GTO linked to collisional tectonics of the North and Central Australian cratons (Bagas et al., 2014).

Geologically, the bulk of the gold mineralisation in the GTO is contained within the c. 1912 to 1838 Ma Tanami Group, a thick sequence of marine turbidite, chert, ironstone and contemporaneous mafic volcanic flows. The Tanami Group, which unconformably overlies Neoarchean basement, was deposited in a rift-related, continental back-arc environment and subsequently deformed by the first phase of the Tanami Orogeny ($DGTO_1$) between c. 1840 and 1825 Ma. Post-Tanami Group sedimentation, represented by the unconformably overlying siliciclastic sedimentary and felsic volcanic sequences of the c. 1825 to 1810 Ma Mount Winnecke and Ware groups was terminated by the second phase of the Tanami Orogeny ($DGTO_{2+3}$). This tectonothermal event, typically referred to as the Stafford Event, occurred between c. 1810 and 1790 Ma, synchronous with widespread intrusion of the 1825 to 1790 Ma Birthday, Frederick and Grimwade granite suites and gold mineralisation at c. 1795 Ma (Joly et al., 2012; Bagas et al., 2014; Roshanravan et al., 2020; Crawford et al., 2024).

Overall, the GTO recorded an intricate history of (i) basin development and inversion, deformation by folding and faulting, metamorphism up to amphibolite facies grade, and intrusion by gabbroic dykes and granitic bodies. The gold mineralisation, commonly categorized as orogenic in nature, was spatially and temporally linked to collisional tectonics in a back-arc environment above a north-dipping subduction zone, in particular late-stage compression and coeval magmatism at c. 1795 Ma (Joly et al., 2012; Bagas et al., 2014; Roshanravan et al., 2020).

Table 1
List of competent predictor maps adapted from Roshanravan et al. (2020).

Critical processes	Predictor maps	Rationale	Brief description
Source	None	No mappable evidence of source processes given a deep crustal and/or upper mantle source. Widespread distribution of and similar nature of gold occurrences and absence of vertical and lateral zoning rules out intrusive point sources.	
Transport	Domains of greater metallogenic trend line density	Mappable evidence of gold-related fluid flow and structures that controlled it.	Metallogenic trend lines correspond to directions of maximum continuity of gold occurrence alignment and were interpreted to represent long-lived, permeable basement structures.
	Domains of greater metallogenic trend line intersection density		As above. However, fluid flow was likely enhanced where long-lived, permeable basement structures intersect each other.
	Proximity to D1 and D2 folds		Folds have abundance and proximity relationships with the known gold occurrences and were interpreted to represent domains of strike-parallel directional permeability.
	Proximity to major faults		Deep-seated, mantle-tapping, 1st-order faults typically facilitate mantle-crust connectivity.
	Proximity to faults		2nd- and 3rd-order faults typically act as important camp- to district-scale fluid pathways.
	Domains of greater fault density		As above. However, greater fault density is typically a sign of greater dilation, brecciation and fluid flow.
	Proximity to domains of remanent magnetisation		Domains of remanent magnetization have abundance and proximity relationships with the known gold occurrences and were interpreted to represent fluid pathways.
	Proximity to gravity worms		Gravity worms with the highest levels of upward continuation were interpreted to represent long-lived, permeable basement structures.
	Proximity to gravity lineaments		Gravity lineaments were interpreted to represent long-lived, permeable basement structures.
	Proximity to pseudogravity worms		Pseudogravity worms with the highest levels of upward continuation were interpreted to represent upper-crustal faults and shear zones.
Trap	Proximity to compositionally heterogeneous rock packages	Mappable evidence of structurally and chemically prepared sites of transient, highly focused fluid flow	Compositionally heterogeneous rock packages are more (i) susceptible to localized fracturing, dilation and permeability and (ii) likely to bear strong chemical gradients.
	Proximity to fault/fold intersections		Intersections between faults and folds represent highly favorable trap sites that are often mineralised in orogenic gold systems worlwide.
	Domains of greater fault intersections density		Domains of greater fault intersections density are often mineralised in orogenic gold systems worlwide.
	Domains of greater lithological contact density		Domains of greater lithological contact density are often mineralised in orogenic gold systems worlwide.
	Proximity to contacts between the Dead Bullock and Killi Killi formations		These contacts represent domains of high rheological ± chemical contrast, which are often mineralised in orogenic gold systems worlwide.
	Proximity to potential host lithologies		These lithologies, which comprise all pre-Mesoproterozoic lithologies, represent the overall gold permissive tract.
Deposition	Proximity to geochemical anomalies	Mappable evidence of (physico-)chemical destabilisation of gold-bearing fluids	Anomalous concentrations of gold and pathfinder elements (As, Ag, Bi, Cu, Mo and Sb) in soils, rocks and drill holes.
	Domains of greater quartz vein density		Evidence of hydrothermal activity and quartz vein deposition.
	Domains of greater mafic dyke density		Mafic dykes host important gold deposits possibly because they not only present lithological competency but also geochemical (redox) gradients.

Note: Readers are referred to Roshanravan et al. (2020) for a more comprehensive discussion of the predictor maps.

2.2. Exploration targeting model

Based on a comprehensive review and first-hand knowledge of gold mineralisation in the GTO, Roshanravan et al. (2020) developed a process-based targeting model in the framework of a mineral systems approach (Table 1).

In this targeting model, the critical ore-forming processes are akin to those typically proposed for orogenic gold deposits (Groves et al., 2020) whereby gold mineralisation occurred in the late phase of the Tanami Orogeny, presumably through far-field stress transfers linked to the accretion of several ribbon-like micro-continents along the southern margin the North Australian Craton during the assembly of the super-continent Nuna (Joly et al., 2012; Bagas et al., 2014; Betts et al., 2016). Whilst the source of the gold in the GTO is unknown, a deeper crustal or upper mantle source region is consistent with the available geological and isotopic evidence (Joly et al., 2012) as well as the orogenic gold deposit model in which the gold-bearing fluids are regarded as the products of deep-seated magmatic or metamorphic devolatilization in subduction-related tectonic environments (Groves et al., 2020).

Structure and lithology are the primary controls on gold mineralisation in the GTO (Joly et al., 2012; Roshanravan et al., 2020; Crawford et al., 2024). Structure, such as shear zones, fault-fracture systems, folds and geological contacts, is important at all scales as structure controls both the transport and depositional processes of the gold-bearing fluids, creating structural pathways of high permeability and focusing deposition to structurally controlled locations (Vearncombe and Zelic, 2015; Groves et al., 2020). Lithology, on the other hand, imparts a critical control on the style, grade and size of the gold mineralisation. A case in point are the chemically reactive sedimentary rocks of the Dead Bullock Formation (Tanami Group), which host the Dead Bullock Soak goldfield, the largest known gold accumulation in the GTO (Crawford et al., 2024).

2.3. Exploration stage

Whilst over 175 gold occurrences have been identified since gold was first discovered in 1900 and despite the presence of several advanced gold projects and a significant active mining operation (i.e., Newmont Corporation's Tanami mine with annual production of >480,000 oz of gold in 2022–23: Northern Territory Government, 2024), the GTO still presents as a largely greenfields environment because of widespread transported cover, lack of any significant prospecting and exploration activities until well into the 20th century, challenging logistics in remote desert country, and poor understanding of the largely concealed and heavily folded and dismembered geology.

3. Methods

3.1. Best-worst method (BWM)

The best worst-method (BWM), a comparison-based MCDM technique introduced by Rezaei (2015), presents a new and effective tool for allocating weights to predictor map classes. The BWM approach has been rendered applicable due to a number of critical features of which the following are deemed the most important (Rezaei, 2015; Stević et al., 2017): (i) Merely integer numbers are utilised when comparing the decision criteria in pairs, (ii) the credibility of the determined weight coefficients is higher than that of similar procedures, (iii) pairwise comparisons are substantially diminished as opposed to prevalent comparison-based techniques like AHP, and (iv) it can either be combined with other multi-criteria techniques or function autonomously for weight computation.

In order to acquire the weights of predictor maps in BWM, the following procedure is applied (Rezaei, 2015).

- Step 1. Establish a collection of decision criteria $\{DC_1, DC_2, ..., DC_n\}$ to be employed in order to accomplish the ultimate decision objective.
- Step 2. Make a list of all the possible decision criteria and rank them from worst (i.e., least important) to best (i.e., most important). There is no comparison at this step; the best and worst decision criteria are only defined by decision-makers.
- Step 3. Give the best decision criterion a priority ranking from 1 to 9 to indicate its position relative to the other decision criteria. This would lead to the following best-to-others (BO) vector:

$$M_B = (m_{B1}, m_{B2}, ..., m_{Bn}) \tag{1}$$

In the given vector, m_{Bj} reflects the superiority of the best decision criterion B over the decision criterion j with $m_{BB} = 1$.

- Step 4. Give all the decision criteria a priority ranking from 1 to 9 to indicate their position relative to the worst decision criterion. This would lead to the following others-to-worst (OW) vector:

$$M_W = (m_{1W}, m_{2W}, ..., m_{nW})^T \tag{2}$$

In the given vector, m_{jw} reflects the superiority of the decision criterion j over the worst decision criterion W with $m_{WW} = 1$.

- Step 5. Define the optimal weights $(W_1^*, W_2^*, ..., W_n^*)$ and ξ^* by solving the given problem:

$$\begin{aligned} &min \xi \\ &\text{s.t.} \\ &\left|W_B - m_{Bj} W_j\right| \le \xi, \text{for all} j \\ &\left|W_j - m_{jW} W_W\right| \le \xi, \text{for all} j \\ &\sum_j W_j = 1 \\ &W_j \ge 0, \text{for all} j \end{aligned} \tag{3}$$

Once ξ^* is acquired, the following equation can be utilised to compute the consistency ratio:

$$\text{Consistency Ratio} = \frac{\xi^*}{\text{Consistency Index}} \tag{4}$$

where consistency index is specified according to Table 2. The consistency ratio is a numerical value that falls between 0 and 1. Values that are close to 0 indicate a higher level of consistency, whilst values that are closer to 1 indicate a lower level of consistency. For a more detailed account of the BWM technique, readers are directed to Rezaei (2015).

3.2. Measurement of alternatives and ranking according to COmpromise solution (MARCOS)

The MARCOS approach, which operates based on defining the correlation between reference values, namely an ideal solution (*AI*) and an anti-ideal solution (*AAI*), and alternatives, is a matrix-based technique in which the utility functions of alternatives are defined pursuant to the established correlations and a compromise ranking is constructed with regard to an *AI* and *AAI*. Utility functions that determine decision preferences indicate the position of an alternative with respect to an *AI*

Table 2
Consistency index.

a_{BW}	1	2	3	4	5	6	7	8	9
Consistency index (maxξ)	0.00	0.44	1.00	1.63	2.30	3.00	3.73	4.47	5.23

and *AAI*. The best alternative is the one that is furthest from the *AI* and simultaneously closest to the *AAI*. The advantages of this approach are (Stević et al., 2020): (i) the ability to keep the technique stable whilst considering an extensive collection of alternatives and decision criteria, (ii) the preposition of a modern procedure for defining the functions of utility and their aggregation, (iii) the examination of an anti-ideal solution (*AAI*) and an ideal solution (*AI*) from the beginning of forming an initial matrix, (iv) the definition of the degree of utility with regard to both *AI* and *AAI*, (v) the algorithm's flexibility in terms of the capability to analyse expert preferences irrespective of the scale type and (vi) the high reliability of the results of this technique due to the fusion of the results of the reference point sorting and ratio approaches.

The algorithm of the MARCOS approach is executed to rank alternatives as follows (Stević et al., 2020):

- Stage 1. Form an initial decision matrix, including m alternatives $\{b_1, b_2, ..., b_m\}$ and n decision criteria $\{DC_1, DC_2, ..., DC_n\}$:

$$B = \begin{bmatrix} b_{11} & b_{12} & \cdots & b_{1n} \\ b_{21} & b_{22} & \cdots & b_{2n} \\ \vdots & \vdots & \cdots & \vdots \\ b_{m1} & b_{m2} & \cdots & b_{mn} \end{bmatrix} = \left[b_{ij}\right]_{m\times n} \tag{5}$$

where the amount of alternative i in relation to decision criterion j is denoted by b_{ij}. Here n denotes the number of spatial proxies (i.e., predictor maps) and m is the cell number encompassing the study area.

- Stage 2. Define the ideal solution (*AI*) and anti-ideal solution (*AAI*) to form an extended initial (EI) matrix:

$$B^{*} = \begin{matrix} AAI \\ A_1 \\ A_2 \\ \vdots \\ A_m \\ AI \end{matrix} \begin{bmatrix} b_{aai1} & b_{aai2} & \cdots & b_{aain} \\ b_{11} & b_{12} & \cdots & b_{1n} \\ b_{21} & b_{22} & \cdots & b_{2n} \\ \vdots & \vdots & \cdots & \vdots \\ b_{m1} & b_{m2} & \cdots & b_{mn} \\ b_{ai1} & b_{ai2} & \cdots & b_{ain} \end{bmatrix} \tag{6}$$

The *AI* is the best alternative, whereas the *AAI* is an alternative with the worst feature. The following equations are utilised to ascertain *AAI* and *AI* based on the criteria's nature:

$$AAI = max\left(b_{ij}\right)\ ;\ AI = min\left(b_{ij}\right) \tag{7}$$

$$AAI = min\left(b_{ij}\right)\ ;\ AI = max\left(b_{ij}\right) \tag{8}$$

Eqs. (7) and (8) are utilised for the criterion with minimal preferable value and the criterion with maximal preferable value, respectively.

- Stage 3. Normalize the EI matrix (B^{*}). Eqs. (9) and (10) are utilised to obtain the elements of the normalized matrix $N = \left[n_{ij}\right]_{m\times n}$:

$$n_{ij} = \frac{b_{aij}}{b_{ij}} \tag{9}$$

Table 3
Contingency table of ROC analysis for specifying quantities of correct rejections (*C*), misses (*M*), false alarms (*F*) and hits (*H*).

Predictor map	Training samples	
	Deposits (1)	Non-deposits (0)
Modeled as prospective for the targeted deposit type (1)	H	F
Modeled as non-prospective for the targeted deposit type (0)	M	C

Table 4
AUC values for competent predictor maps.

Competent predictor maps	AUC
Proximity to D1 and D2 folds (DC_1)	0.88
Proximity to faults (Vanderberg) (DC_2)	0.81
Domains of greater fault density (Vanderberg) (DC_3)	0.84
Proximity to major faults (DC_4)	0.89
Proximity to fault/fold intersections (DC_5)	0.75
Domains of greater fault intersections density (Vanderberg) (DC_6)	0.76
Proximity to gravity lineaments (DC_7)	0.73
Domains of greater metallogenic trend line intersection density (DC_8)	0.88
Proximity to gravity worms (DC_9)	0.53
Proximity to contacts between the Dead Bullock and Killi Killi formations (DC_{10})	0.75
Proximity to lithologically heterogeneous rock packages (DC_{11})	0.96
Proximity to potential host lithologies (DC_{12})	0.99
Domains of greater quartz vein density (DC_{13})	0.86
Domains of greater lithological contact density (DC_{14})	0.85
Domains of greater mafic dyke density (DC_{15})	0.69
Domains of greater metallogenic trend line density (DC_{16})	0.89
Proximity to pseudogravity worms (DC_{17})	0.73
Proximity to domains of remanent magnetization (DC_{18})	0.88
Proximity to geochemical anomalies (DC_{19})	0.86

$$n_{ij} = \frac{b_{ij}}{b_{aij}} \tag{10}$$

where elements b_{aij} and b_{ij} indicate the elements of the matrix B^{*}. Eqs. (9) and (10) are utilised, respectively, for the criteria with minimal and maximal preferable values.

- Stage 4. Determine the weighted matrix $D = \left[d_{ij}\right]_{m\times n}$. This matrix (Eq. (11)) is acquired by multiplying the weight vector of decision criteria $W = [w_1, w_2, ..., w_n]$ that can be obtained by objective or subjective weighting methods with the normalized matrix N.

$$d_{ij} = n_{ij} \times w_j \tag{11}$$

- Stage 5. Compute the utility degree of alternatives *Ei*. Computing an alternative's utility degrees with regard to the *AI* and *AAI* is done, respectively, using Eqs. (12) and (13):

$$E_i^{+} = \frac{S_i}{S_{ai}} \tag{12}$$

$$E_i^{-} = \frac{S_i}{S_{aai}} \tag{13}$$

As shown in Eq. (14), S_i $(i = 1, 2, ..., m)$ in the above equations indicates the summation of the elements of the weighted matrix D.

$$S_i = \sum_{i=1}^{m} d_{ij} \tag{14}$$

- Stage 6. Define the alternatives' utility functions $f(E_i)$. The observed alternative's compromise with regard to the *AAI* and *AI* is referred to as the utility function, which is defined as follows:

$$f(E_i) = \frac{E_i^{+} + E_i^{-}}{1 + \frac{1-f\left(E_i^{+}\right)}{f\left(E_i^{+}\right)} + \frac{1-f\left(E_i^{-}\right)}{f\left(E_i^{-}\right)}} \tag{15}$$

In the above equation, the utility functions with regard to the *AI* and *AAI* are, respectively, denoted as $f\left(E_i^{+}\right)$ and $f\left(E_i^{-}\right)$. Eqs. (16) and (17) are utilised, respectively, to define utility functions with regard to the *AI* and *AAI*.

$$f\left(E_i^{-}\right) = \frac{E_i^{+}}{E_i^{+} + E_i^{-}} \tag{16}$$

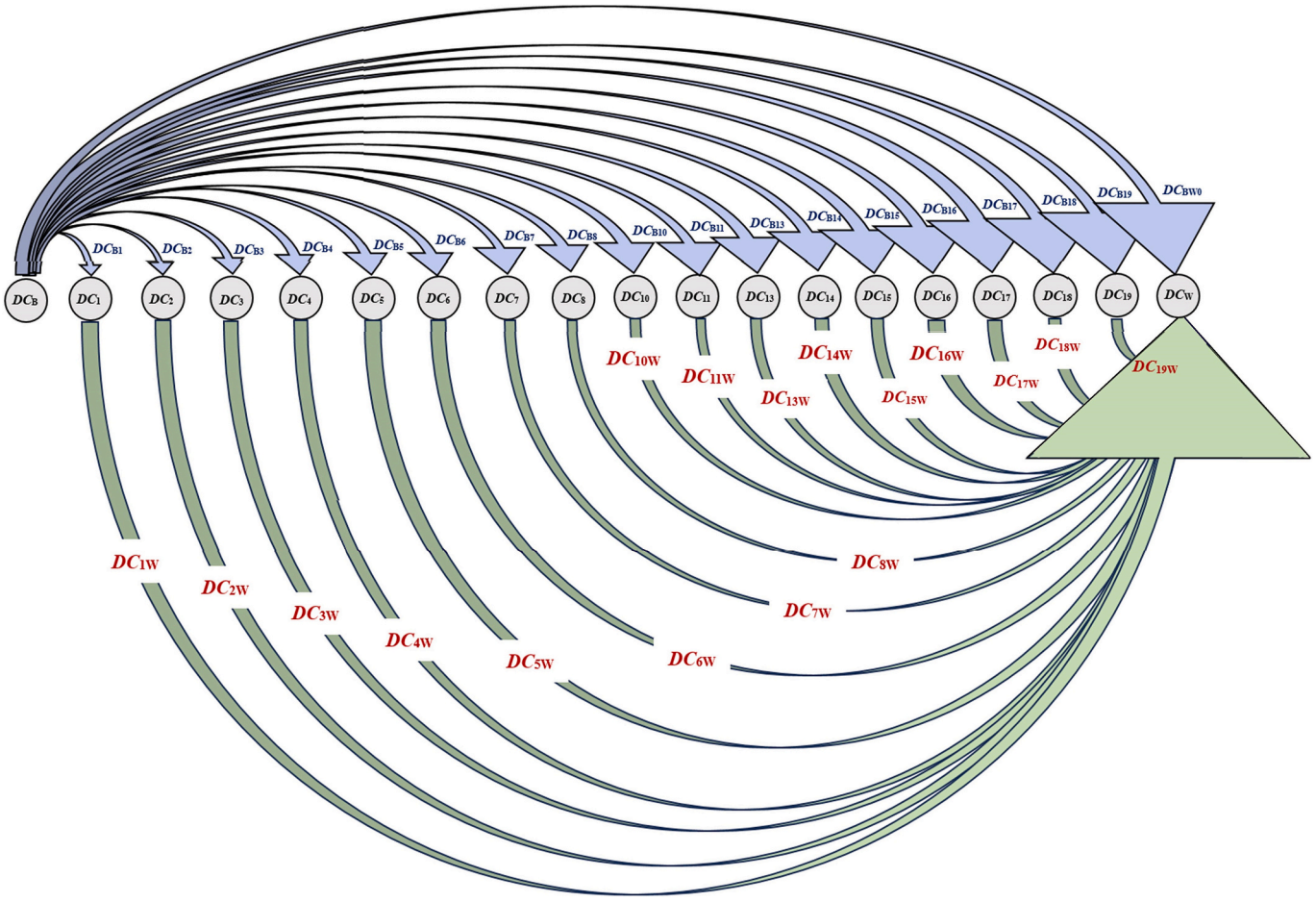

Fig. 2. Reference comparisons: $DC_{B(12)}$ = proximity to potential host lithologies, DC_1 = proximity to D1 and D2 folds, DC_2 = proximity to faults (Vanderberg), DC_3 = domains of greater fault density, DC_4 = proximity to major faults, DC_5 = proximity to fault/fold intersections, DC_6 = domains of greater fault intersections density, DC_7 = proximity to gravity lineaments, DC_8 = domains of greater metallogenic trend line intersection density, DC_{10} = proximity to contacts between the Dead Bullock and Killi Killi formations, DC_{11} = proximity to lithologically heterogeneous rock packages, DC_{13} = domains of greater quartz vein density, DC_{14} = domains of greater lithological contact density, DC_{15} = domains of greater mafic dyke density, DC_{16} = domains of greater metallogenic trend line density, DC_{17} = proximity to pseudogravity worms, DC_{18} = proximity to domains of remanent magnetization, DC_{19} = proximity to geochemical anomalies and $DC_{W(9)}$. The proximity to potential host lithologies and proximity to geochemical anomalies are the most significant and the least significant decision criteria, respectively.

Table 5
Best-to-others pairwise comparison vector based on the *AUC* index.

Decision criteria (predictor maps)	DC_B (12)	DC_1	DC_2	DC_3	DC_4	DC_5	DC_6	DC_7	DC_8	DC_{10}	DC_{11}	DC_{13}	DC_{14}	DC_{15}	DC_{16}	DC_{17}	DC_{18}	DC_{19}	DC_W (9)
Preference of the best decision criterion over the all other decision criteria	1	3	4	4	3	5	5	6	3	5	2	3	3	6	3	6	3	3	9

$$f\left(E_i^+\right) = \frac{E_i^-}{E_i^+ + E_i^-} \tag{17}$$

- Stage 7. Rank the alternatives pursuant to the utility function's ultimate values. In this study, the alternatives with higher utility function values are more favorable for the targeted deposit. Readers are directed to Stević et al. (2020) for a more detailed account of the MARCOS technique.

3.3. The index of the area under the receiver operating characteristic curve (AUC)

The index of *AUC* is determined pursuant to the receiver operating characteristic (ROC) analysis applying various values of threshold to a continuous spatial proxy, pursuant to which the quantities of correct rejections (C), misses (M), false alarms (F) and hits (H) are allocated to each cell or pixel according to the matrix of confusion in Table 3 (cf. Zou et al., 2007; Parsa et al., 2018). The ROC curve depicts the TP_r (true positive rate) and FP_r (false positive rate), respectively, on the horizontal and vertical axes. The FP_r (also referred to as "1 – specificity") is $F/F + C$, or the number of non-prospect locations (NPLs) erroneously discerned as a mineralisation event. The TP_r (also referred to as "sensitivity") is

Table 6
Others-to-worst pairwise comparison vector based on the *AUC* index.

Decision criteria (predictor maps)	Preference of the all other decision criteria over the worst decision criterion
$DC_{W\ (9)}$	1
DC_1	7
DC_2	6
DC_3	6
DC_4	7
DC_5	5
DC_6	5
DC_7	4
DC_8	7
DC_{10}	5
DC_{11}	8
DC_{13}	7
DC_{14}	7
DC_{15}	4
DC_{16}	7
DC_{17}	4
DC_{18}	7
DC_{19}	7
$DC_{B\ (12)}$	9

Table 7
Optimal weights (W^*) derived from the BWM approach.

Competent predictor maps	W^*	ξ^*
Proximity to D1 and D2 folds (DC_1)	0.059	0.032
Proximity to faults (Vanderberg) (DC_2)	0.044	
Domains of greater fault density (DC_3)	0.044	
Proximity to major faults (DC_4)	0.059	
Proximity to fault/fold intersections (DC_5)	0.035	
Domains of greater fault intersections density (DC_6)	0.035	
Proximity to gravity lineaments (DC_7)	0.029	
Domains of greater metallogenic trend line intersection density (DC_8)	0.059	
Proximity to gravity worms (DC_9)	0.013	
Proximity to contacts between the Dead Bullock and Killi Killi formations (DC_{10})	0.035	
Proximity to lithologically heterogeneous rock packages (DC_{11})	0.088	
Proximity to potential host lithologies (DC_{12})	0.145	
Domains of greater quartz vein density (DC_{13})	0.059	
Domains of greater lithological contact density (DC_{14})	0.059	
Domains of greater mafic dyke density (DC_{15})	0.029	
Domains of greater metallogenic trend line density (DC_{16})	0.059	
Proximity to pseudogravity worms (DC_{17})	0.029	
Proximity to domains of remanent magnetization (DC_{18})	0.059	
Proximity to geochemical anomalies (DC_{19})	0.059	

$H/H+M$, or the number of prospect locations (PLs) correctly modeled as a mineralisation event. The curve of ROC is created by connecting the diverse TP_r and FP_r values specified by applying the various values of threshold to the predictor map.

4. Mineral potential modelling (MPM)

4.1. Development of BWM-MARCOS model

As a first step, the BWM approach was used to objectively determine the weights of the decision criteria relating to the 19 competent predictor maps formerly developed and described by Roshanravan et al. (2020) (Table 1). To achieve this, we utilised the *AUC* index to specify predictor map weights as well as the best and worst predictor maps (Table 4), namely "proximity to gravity worms" ($AUC = 0.53$) and "proximity to potential host lithologies" ($AUC = 0.99$) (Fig. 2).

Next, the BO and OW pairwise comparison vectors were specified (Tables 5 and 6) pursuant to the *AUC* values listed in Table 4. Therefore, the problem (3) could be written as follows:

$$\begin{aligned}
&min\xi\\
&\text{s.t.}\\
&|W_{12}-3W_1|\le\xi,\text{for all}j\\
&|W_{12}-4W_2|\le\xi,\text{for all}j\\
&|W_{12}-4W_3|\le\xi,\text{for all}j\\
&\quad\vdots\\
&|W_{12}-3W_{19}|\le\xi,\text{for all}j\\
&|W_1-7W_9|\le\xi,\text{for all}j\\
&|W_2-6W_9|\le\xi,\text{for all}j\\
&|W_3-6W_9|\le\xi,\text{for all}j\\
&\quad\vdots\\
&|W_{19}-7W_9|\le\xi,\text{for all}j\\
&\sum_j W_j=1\\
&W_j\ge 0,\text{for all}j
\end{aligned}\tag{18}$$

Subsequently, the optimal weights $\left(W_B^*, W_1^*, \ldots, W_W^*\right)$ and ξ^* were determined by solving the above equation as shown in Table 7. For $a_{BW} = a_{129} = 9$, the obtained consistency index was 5.23 (Table 2) whilst the consistency ratio was $0.032/5.23 = 0.006$, indicating excellent consistency. After assigning weights to the predictor maps, the MARCOS approach was utilised to rank the alternatives. The initial decision matrix obtained in this step $B_{1162249\times19}$ contained 1,162,249 alternatives, each of which linked to an individual cell with a certain coordinate in the corresponding predictor maps, and 19 decision criteria. The alternatives were then ranked via the MARCOS step-by-stage process outlined in Section 3.2 (Fig. 3).

Fig. 4 illustrates the resulting BWM-MARCOS model of orogenic gold potential in the GTO.

4.2. Evaluation of BWM-MARCOS model

After having developed the BWM-MARCOS model (Fig. 4), its performance was appraised using the training data of Roshanravan et al. (2020) as control points. The training data comprise of 150 prospect sites (i.e., gold deposits and occurrences, significant mineralised drill intercepts) and 150 non-prospect sites. Non-prospect sites were selected pursuant to the following rules: (i) They ought to be outside the gold permissive tract, (ii) they ought to be distant from the prospect sites, and (iii) their spatial distribution ought to be random. As part of this step, we utilised the improved plot of prediction-area (P-A) as a powerful validation tool that can simultaneously and reliably appraise three principal parameters; viz. the (i) prediction rate of PLs, (ii) prediction rate of NPLs and (iii) occupied area of modeled exploration targets (Roshanravan et al., 2019). Class thresholds (Fig. 5a) were specified using the fractal technique of concentration-area for generating a classified potential model (Fig. 5b). According to Cheng et al. (1994), the scale-invariant concentration-area fractal approach can be defined as follows:

$$A(\ge c)\propto c^{-\alpha}\tag{19}$$

where $A \ge c$ indicates the area with values greater than or equal to c and α is the fractal dimension. The fractal dimension can be estimated by slopes of straight lines fitted on the log-log plot of $A \ge c$ versus c. Ultimately, the improved plot of P-A was developed by incorporating three curves, viz. the occupied area curve and the prediction rate curves of NPLs and PLs plotted against their corresponding prospectivity classes as per the BWM-MARCOS potential model (Fig. 5c). As characterised by the efficiency statistics presented in Table 8 and the improved plot of P-A in Fig. 5c, the overall performance (O_p) of the BWM-MARCOS prospectivity model is 0.54. As such, it boasts a higher performance value than any of the continuous (i.e., geometric average, data-driven index overlay and fuzzy gamma), knowledge-driven (i.e., fuzzy inference system) and data-driven (i.e., feed-forward deep neural network and 'original' random forest) mineral prospectivity maps formerly

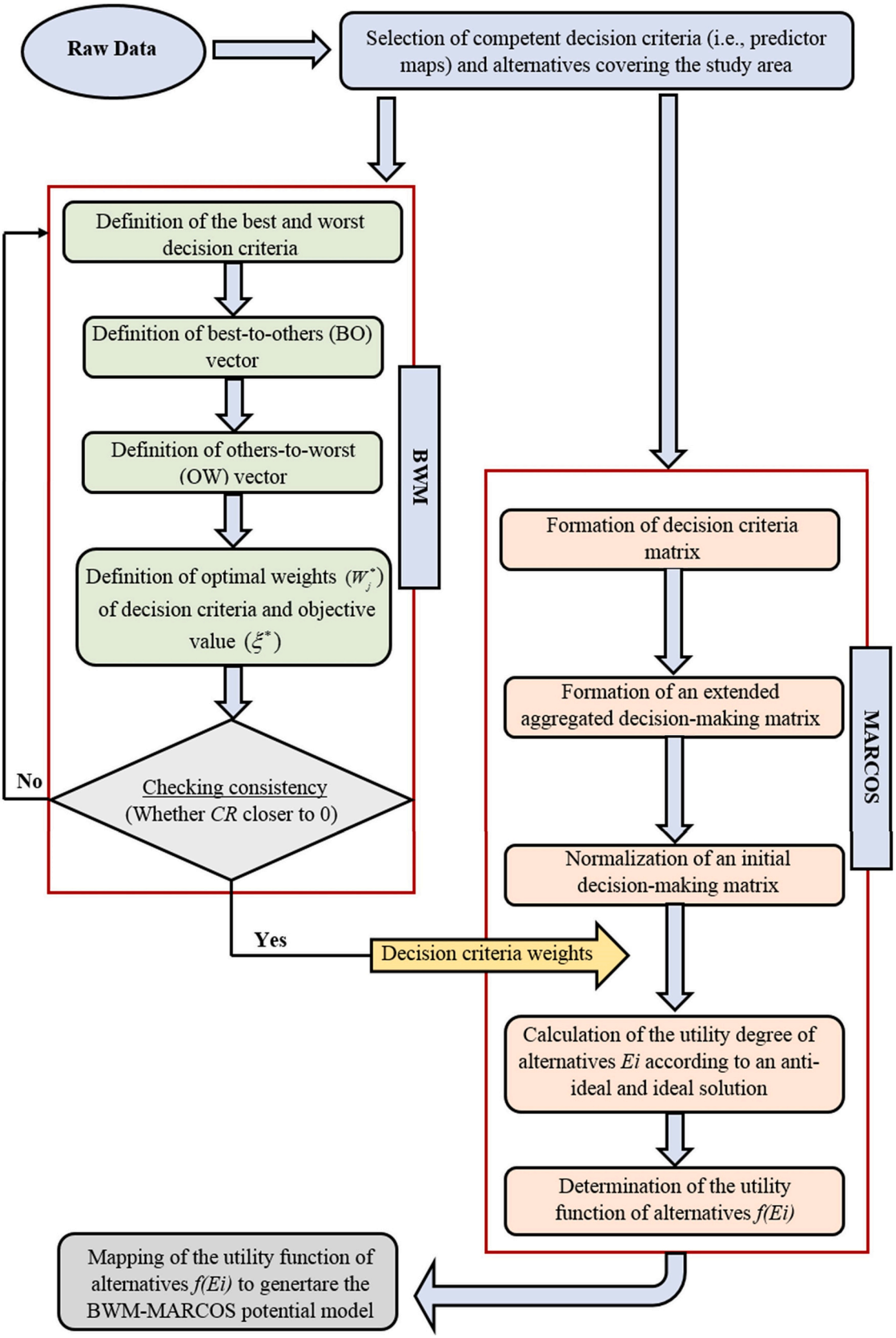

Fig. 3. Flowchart illustrating the hybrid BWM-MARCOS approach.

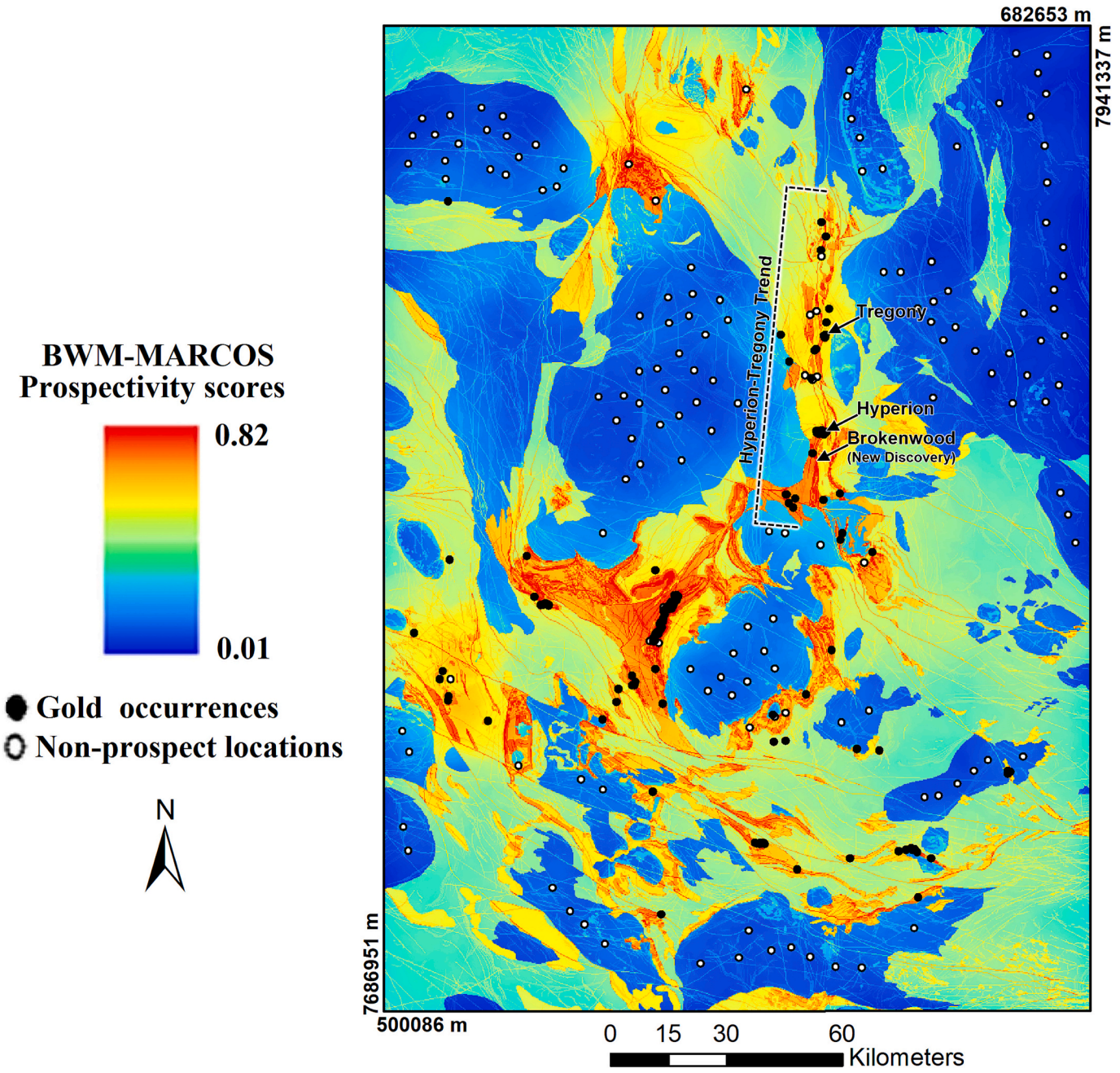

Fig. 4. BWM-MARCOS potential map generated by combining the 19 competent predictor maps. The gold trend and occurrences referred to in Section 5.4 are labelled.

developed by Roshanravan et al. (2020, 2023b), utilising the same underlying predictor maps, study area and targeting model.

5. Discussion

5.1. Generation and application of targeting model and predictor maps

Building a targeting model for MPM consists of two pivotal tasks (McCuaig et al., 2010; Joly et al., 2012):

- Identification of the critical ore-forming processes, their constituent processes, the geological expressions of the constituent processes and their mappable expressions (also referred to as targeting criteria or elements) that serve to demarcate the targeting elements either directly or by proxy.
- Translation of the mappable targeting criteria into predictor maps for use in MPM.

These tasks are very important, not only because the quality of MPM is highly contingent upon the quality of the underlying conceptual model and generation of suitable spatial proxies (Kreuzer et al., 2020) but also because most stochastic uncertainties arise from the improper selection of predictor maps (An et al., 1994). In our experience, the mineral systems approach (Wyborn et al., 1994; McCuaig et al., 2010) provides an ideal framework for building an effective targeting model and competent predictor maps in that it offers a systematic, probabilistic framework (Kreuzer et al., 2008). In addition, it is recommended here that, in brownfields environments, where a sufficiently large number of mineral occurrences is typically available in support of spatial numerical analysis, statistical indices such as the area under the receiver operating

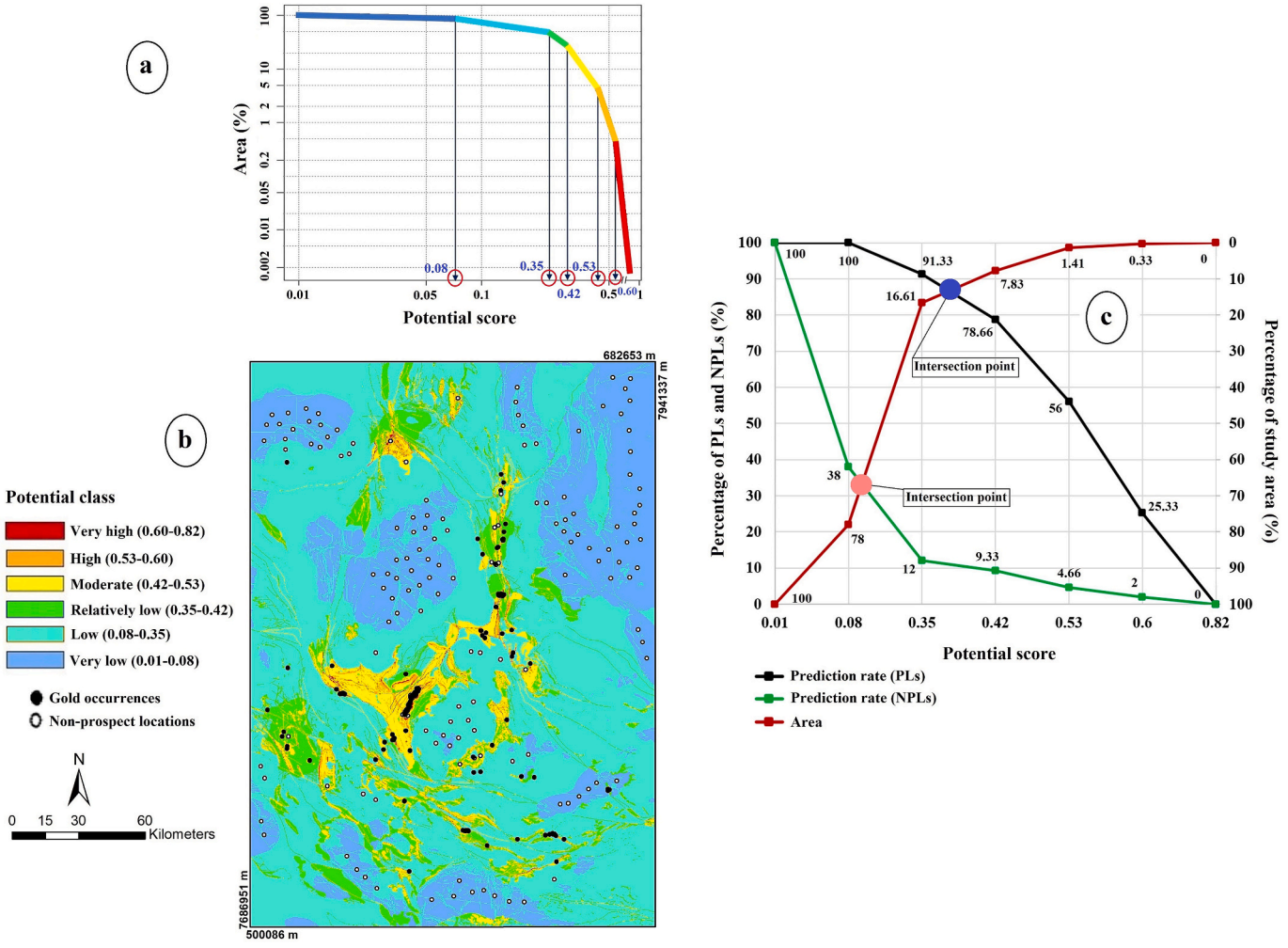

Fig. 5. Validation of potential scores from Fig. 4: (a) Concentration-area fractal model, (b) Classified potential map and (c) improved prediction-area plot.

Table 8
Efficiency statistics for the BWM-MARCOS model.

Parameter	BWM-MARCOS model
Hits (*Pm*)	87
False Alarms (*Pn*)	33
Misses (100-*Pm*)	13
Correct Rejections (100-*Pn*)	67
True Positive Rate (*TPr*)	0.87
False Positive Rate (*FPr*)	0.33
Overall Performance (*Op*)	0.54

characteristic curve (*AUC*) or normalized density (N_d) be computed to ascertain adequate predictor map performance (Mihalasky and Bonham-Carter, 2001; Nykänen et al., 2015). Here, we employed a carefully developed targeting model considered by Roshanravan et al. (2020) to reflect the critical geological processes that controlled orogenic gold mineralisation in the GTO (Table 1) in conjunction with 19 competent predictor maps previously developed and tested by Roshanravan et al. (2020). The predictor maps were generated neither expert opinion nor mineral occurrences data. Therefore, continuous spatial evidence values have greater predictive ability than discretised ones (Yousefi et al., 2019).

5.2. Weighing and integration of predictor maps

Another pivotal task in MPM is the application of robust techniques to weigh and integrate predictor maps. The MARCOS technique refreshing the domain of MCDM offers an algorithm that can analyse the degree of correlation between anti-ideal and ideal values and alternatives presents a new, effective, straightforward and robust method for combining decision criteria or predictor maps (Stević et al., 2020). In cases where the MARCOS method fails to generate a well-performing mineral potential model, for example in cases where input is reliant on expert knowledge, the combination of the MARCOS and BWM methods is likely to yield a more effective model. Additionally, relevant studies demonstrated that hybrid MCDM typically outperform single MCDM techniques with regards to identifying prospective target areas (Aryafar and Roshanravan, 2020, 2021; Feizi et al., 2021; Mohammadzadeh et al., 2021; Maghsoudi Moud et al., 2022; Riahi et al., 2023a, 2023b). Whilst the subjective nature of the hybrid BWM-MARCOS approach presented in this study is not without its flaws, it serves to mitigate some of the impediments affecting the prevailing approaches to knowledge-driven MPM. To mitigate any flaws, the authors applied the *AUC* index designed to objectively assess the weights of predictor maps as well as the worst and best decision criteria.

5.3. State-of-the art methods for MPM and model performance and comparison

Current state-of-the-art supervised techniques for MPM comprise machine learning techniques, such as support vector machines (Roshanravan et al., 2021; Lou and Liu, 2023), the random forest algorithm (Sun et al., 2019; Roshanravan et al., 2023a), gradient boosting

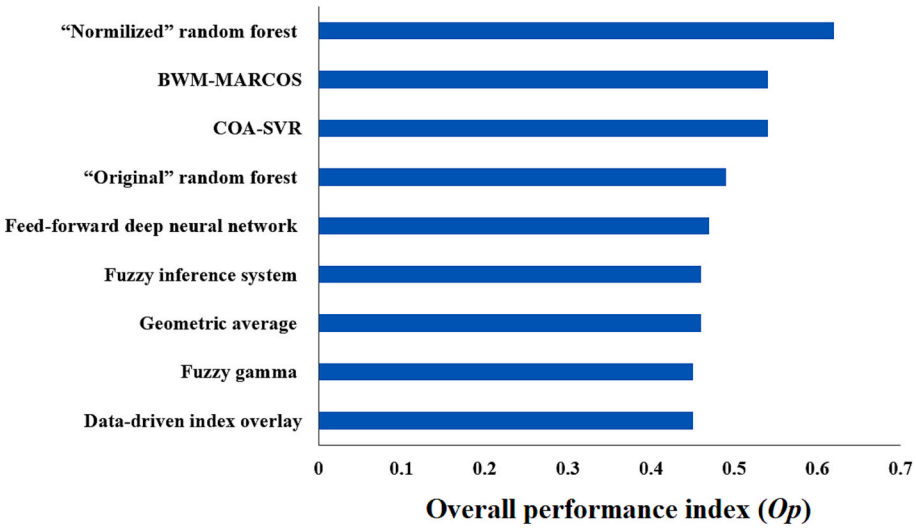

Fig. 6. Comparison of nine GTO gold prospectivity models generated by Roshanravan et al. (2020, 2021, 2023a, 2023b, this study).

machines (Parsa, 2021; Lou and Liu, 2023), and deep learning techniques, such as feed-forward deep neural network (Roshanravan et al., 2023b), convolutional neural network (Lou and Liu, 2023) and deep belief networks (Keykhay-Hosseinpoor et al., 2024). As depicted in Fig. 6, whilst the knowledge-driven BWM-MARCOS approach relies on expert judgment, its performance is better than that of data-driven (supervised) MPM techniques such as the feed-forward deep neural network and 'original' random forest models of Roshanravan et al. (2020, 2023b) and similar to that of the COA-SVR model of Roshanravan et al. (2021). Furthermore, the performance of the BWM-MARCOS technique is better than that of continuous (i.e., fuzzy gamma, geometric average and data-driven index overlay), so-called 'fourth generation' MPM methods (Fig. 6).

As illustrated in Fig. 6, the performance rate of the BWM-MARCOS model is similar to that of the COA-SVR model of Roshanravan et al. (2021), which is a data-driven (supervised) MPM technique. The relatively similar performance rate of these different approaches may simply be due to the similarly objective *AUC*-based determination of predictor map weights, acting to reduce stochastic uncertainty linked to expert judgment. The best performer among the nine gold potential models for the GTO (Roshanravan et al., 2020, 2021, 2023b, this study) is the "normalized" RF model (O_p = 0.62), which used transformed spatial proxies (Fig. 6). This superiority may be linked to an inherent property of the RF technique, enabling it to run repeated regression models, thereby improving the outcomes and generating an ultimate output based on the average of the exclusive purified regression models (Breiman, 2001). This capability renders the regression more accurate and enhances the reliability of the spatial prediction compared to other techniques such as the COA-SVR and FF-DNN approaches.

5.4. Mineral exploration implications and feedback loop

From a practical mineral exploration perspective, the MPM completed to date (Roshanravan et al., 2020, 2021, 2023b, this study) has delivered tangible exploration results for Prodigy Gold NL and instilled more confidence in their exploration targeting models. More specifically, the results of the MPM (Prodigy Gold NL, 2023; Orlando, 2023):

- Reinforced Prodigy's confidence to target the Hyperion-Tregony trend, which stood out in the MPM as a clear exploration target.
- Lead Prodigy to target areas within their tenement holdings that had previously been neglected as well as apply for additional exploration tenements over ground where the MPM indicated a high likelihood of gold mineralisation.

Subsequent drilling by Prodigy along the Hyperion-Tregony trend delivered wide, high-grade intercepts at the Hyperion deposit of up to 40 m @ 6.2 g/t Au from 60 m and at the Tregony deposit of up to 6 m @ 15.7 g/t Au from 91 m as well as a new greenfields discovery at Brokenwood where the discovery hole returned 6 m @ 8.1 g/t Au from 98 m (Prodigy Gold NL, 2024) (Figs. 1 and 4). These results also provided important feedback, in particular in regard to real-world MPM performance and improved geological understanding of targeted gold mineral system.

6. Summary and conclusions

Hybrid multi-criteria decision-making (MCDM) is a novel tool in the mineral potential modelling (MPM) toolbox with recent research having demonstrated its strengths and effectiveness. Here we adopted a hybrid MCDM technique known as the Best-Worst Method (BMW) and combined it with the Measurement of Alternatives and Ranking according to COmpromise Solution (MARCOS) technique. The combined "Best-Worst Method-Measurement of Alternatives and Ranking according to COmpromise Solution" (BWM-MARCOS) approach, a newly devised MPM technique, served to (i) map orogenic gold potential in the Granites-Tanami Orogen (GTO) of Australia's Northern Territory and (ii) compare and contrast its performance to that of previous MPM methods applied to the same study area and utilising the same predictor maps and targeting model.

Our appraisal of the gold potential map generated with the novel BWM-MARCOS technique revealed an overall performance index (O_p) value of 0.54, which is a superior result compared to the O_p values of the previously generated knowledge-driven fuzzy inference system (O_p = 0.46), continuous fuzzy gamma (O_p = 0.45), data-driven index overlay (O_p = 0.45) and geometric average (O_p = 0.46) as well as data-driven, feed-forward deep neural network (O_p = 0.47) and "original" random forest (O_p = 0.49) models of Roshanravan et al. (2020, 2023b). In addition, the performance of the new BWM-MARCOS potential model was found to be similar to that of the COA-SVR (O_p = 0.54) model of Roshanravan et al. (2021), a supervised (data-driven) MPM technique.

Last but not least, the prioritised 1st order (top priority) and 2nd order (high priority) targets cover areas that represent a >303 times (i.e., two orders of magnitude) to >93 times (i.e., one order of magnitude) reduction of the search space. The appraisal outcomes, thus, serve to demonstrate that the proposed BWM-MARCOS approach has the ability

to generate a more accurate map of mineral potential by (i) modulating the effects of subjectivity, (ii) reducing uncertainty through the application of simpler computational frameworks and (iii) objectively determining predictor map weights based on their *AUC* values.

CRediT authorship contribution statement

Bijan Roshanravan: Writing – original draft, Visualization, Methodology, Formal analysis, Conceptualization. **Oliver P. Kreuzer:** Writing – review & editing, Methodology, Investigation, Conceptualization. **Amanda Buckingham:** Writing – review & editing, Methodology, Formal analysis, Data curation.

Ethical statement

The authors state that the research was conducted according to ethical standards.

Funding

The authors did not receive any financial support for the research, authorship and/or publication of this article.

Declaration of competing interest

The authors declare that they have no known competing financial interests or personal relationships that could have appeared to influence the work reported in this paper.

Acknowledgments

The authors would like to acknowledge Prodigy Gold NL for providing access to personnel and data. No funding from external organisations was received for this research.

Data availability

The data are available from the authors upon request and pending permission of Prodigy Gold NL.

References

Altay, B.C., Celik, E., Okumus, A., Balin, A., Gul, M., 2023. An integrated interval type-2 fuzzy BWM-MARCOS model for location selection of e-scooter sharing stations: the case of a university campus. Eng. Appl. Artif. Intel. 122, 106095.

An, P., Moon, W.M., Bonham-Carter, G.F., 1994. Uncertainty management in integration of exploration data using the belief function. Nonrenewable Resources 3, 60–71.

Aryafar, A., Roshanravan, B., 2020. Improved index overlay mineral potential modeling in brown- and green-fields exploration using geochemical, geological and remote sensing data. Earth Sci. Inf. 1–17.

Aryafar, A., Roshanravan, B., 2021. BWM-SAW: a new hybrid MCDM technique for modeling of chromite potential in the Birjand district, east of Iran. J. Geochem. Explor. 231, 106876.

Bagas, L., Boucher, R., Li, B., Miller, J., Hill, P., Depauw, G., Pascoe, J., Eggers, B., 2014. Paleoproterozoic stratigraphy and gold mineralisation in the Granites-Tanami Orogen, North Australian Craton. Aust. J. Earth Sci. 61, 89–111.

Bahrami, Y., Hassani, H., Maghsoudi, A., 2019. BWM-ARAS: a new hybrid MCDM method for Cu prospectivity mapping in the Abhar area, NW Iran. Spatial Statistics 33, 100382.

Betts, P.G., Armit, R.J., Stewart, J., Aitken, A.R.A., Ailleres, L., Donchak, P., Hutton, L., Withnall, I., Giles, D., 2016. Australia and Nuna. Geol. Soc. Lond. Spec. Publ. 424, 47–81.

Bonham-Carter, G.F., 1994. Geographic Information Systems for Geoscientists: Modelling with GIS. Pergamon, Oxford, p. 398.

Breiman, L., 2001. Random forests. Machine Learning 45, 5–32.

Carranza, E.J.M., 2008. Geochemical anomaly and mineral prospectivity mapping in GIS. In: Handbook of Exploration and Environmental Geochemistry, 11, 351 p.

Celik, E., Gul, M., 2021. Hazard identification, risk assessment and control for dam construction safety using an integrated BWM and MARCOS approach under interval type-2 fuzzy sets environment. Autom. Constr. 127, 103699.

Cheng, Q., Agterberg, F.P., Ballantyne, S.B., 1994. The separation of geochemical anomalies from background by fractal methods. J. Geochem. Explor. 51, 109–130.

Crawford, A.F., Maidment, D.W., Thebaud, N., Masurel, Q., Evans, N.J., 2024. A revised stratigraphic model for the ~1910-1835 Ma Tanami Group, the northern Territory, Australia: implications for exploration targeting. Precambrian Res. 411, 107510.

Deveci, M., Özcan, E., John, R., Pamucar, D., Karaman, H., 2021. Offshore wind farm site selection using interval rough numbers based Best-Worst Method and MARCOS. Appl. Soft Comput. 109, 107532.

Ecer, F., Pamucar, D., 2021. MARCOS technique under intuitionistic fuzzy environment for determining the COVID-19 pandemic performance of insurance companies in terms of healthcare services. Appl. Soft Comput. 104, 107199.

Feizi, F., Karbalaei-Ramezanali, A., Tusi, H., 2017. Mineral potential mapping via TOPSIS with hybrid AHP–Shannon entropy weighting of evidence: a case study for porphyry-cu, Farmahin area, Markazi Province, Iran. Natural Resources Research 26, 553–570.

Feizi, F., Karbalaei-Ramezanali, A.A., Farhadi, S., 2021. FUCOM-MOORA and FUCOM-MOOSRA: new MCDM-based knowledge-driven procedures for mineral potential mapping in greenfields. SN Applied Sciences 3, 1–19.

Ford, A., Hart, C.J., 2013. Mineral potential mapping in frontier regions: a Mongolian case study. Ore Geol. Rev. 51, 15–26.

Forson, E.D., Menyeh, A., 2023. Best worst method-based mineral prospectivity modeling over the Central part of the Southern Kibi-Winneba Belt of Ghana. Earth Science Informatics 16, 1657–1676.

Groves, D.I., Santosh, M., Zhang, L., 2020. A scale-integrated exploration model for orogenic gold deposits based on a mineral system approach. Geosci. Front. 11 (3), 719–738.

Hronsky, J.M., Kreuzer, O.P., 2019. Applying spatial prospectivity mapping to exploration targeting: fundamental practical issues and suggested solutions for the future. Ore Geol. Rev. 107, 647–653.

Joly, A., Porwal, A., McCuaig, T.C., 2012. Exploration targeting for orogenic gold deposits in the Granites-Tanami Orogen: mineral system analysis, targeting model and prospectivity analysis. Ore Geol. Rev. 48, 349–383.

Karbalaei-Ramezanali, A., Feizi, F., Jafarirad, A., Lotfi, M., 2020. Application of Best-Worst method and Additive Ratio Assessment in mineral prospectivity mapping: a case study of vein-type copper mineralization in the Kuhsiah-e-Urmak Area, Iran. Ore Geology Reviews 117, 103268.

Keykhay-Hosseinpoor, M., Porwal, A., Rajendran, K., 2024. Targeting porphyry Cu deposits in the Chahargonbad region of Iran: a joint application of deep belief networks and random forest techniques. Geochemistry, 126155.

Kreuzer, O.P., Etheridge, M.A., Guj, P., McMahon, M.E., Holden, D.J., 2008. Linking mineral deposit models to quantitative risk analysis and decision-making in exploration. Econ. Geol. 103 (4), 829–850.

Kreuzer, O.P., Markwitz, V., Porwal, A.K., McCuaig, T.C., 2010. A continent-wide study of Australia's uranium potential: part I: GIS-assisted manual prospectivity analysis. Ore Geol. Rev. 38, 334–366.

Kreuzer, O.P., Miller, A.V., Peters, K.J., Payne, C., Wildman, C., Partington, G.A., Puccioni, E., McMahon, M.E., Etheridge, M.A., 2015. Comparing prospectivity modelling results and past exploration data: a case study of porphyry Cu–Au mineral systems in the Macquarie Arc, Lachlan Fold Belt, New South Wales. Ore Geol. Rev. 71, 516–544.

Kreuzer, O.P., Buckingham, A., Mortimer, J., Walker, G., Wilde, A., Appiah, K., 2019. An integrated approach to the search for gold in a mature, data-rich brownfields environment: a case study from Sigma-Lamaque, Quebec. Ore Geol. Rev. 111, 102977. https://doi.org/10.1016/j.oregeorev.2019.102977.

Kreuzer, O.P., Yousefi, M., Nykänen, V., 2020. Introduction to the special issue on spatial modelling and analysis of ore-forming processes in mineral exploration targeting. Ore Geol. Rev. 119, 103391.

Kumwenda, J., Betts, P., Armit, R., 2023. Exposing basement terranes of the North Australian Craton. Earth Sci. Rev. 237, 104310.

Lindsay, M., Aitken, A., Ford, A., Dentith, M., Hollis, J., Tyler, I., 2016. Reducing subjectivity in multi-commodity mineral prospectivity analyses: Modelling the west Kimberley, Australia. Ore Geol. Rev. 76, 395–413.

Lou, Y., Liu, Y., 2023. Mineral prospectivity mapping of tungsten polymetallic deposits using machine learning algorithms and comparison of their performance in the Gannan region, China. Earth and Space Science 10, e2022EA002596.

Maghsoudi Moud, F., Abbaszadeh Shahri, A., van Ruitenbeek, F., Hewson, R., van der Meijde, M., 2022. Evaluation of the modified AHP-VIKOR for mapping and ranking copper mineralized areas, a case study from the Kerman metallogenic belt, SE Iran. Arabian Journal of Geosciences 15, 1756.

McCuaig, T.C., Beresford, S., Hronsky, J., 2010. Translating the mineral systems approach into an effective exploration targeting system. Ore Geol. Rev. 38, 128–138.

Mihalasky, M.J., Bonham-Carter, G.F., 2001. Lithodiversity and its spatial association with metallic mineral sites, Great Basin of Nevada. Natural Resources Research 10, 209–226.

Mohammadzadeh, M., Nasseri, A., Mahboubiaghdam, M., Jahangiri, M., 2021. Mineral prospectivity mapping of Cu-Au by integrating AHP technique with ARAS and WASPAS models in the Sonajil area, E-Azerbaijan. Zeitschrift der Deutschen Gesellschaft für Geowissenschaften (ZDGG) 172.

Nguyen, H.Q., Nguyen, V.T., Phan, D.P., Tran, Q.H., Vu, N.P., 2022. Multi-criteria decision making in the PMEDM process by using MARCOS, TOPSIS, and MAIRCA methods. Appl. Sci. 12, 3720.

Northern Territory Government, 2004. Resourcing the Territory – gold. In: Northern Territory Government (NT Geological Survey), Resourcing the Territory Fact Sheet, July 2024, 2 p.

Nykänen, V., Lahti, I., Niiranen, T., Korhonen, K., 2015. Receiver operating characteristics (ROC) as validation tool for prospectivity models—a magmatic Ni–Cu case study from the Central Lapland Greenstone Belt, Northern Finland. Ore Geol. Rev. 71, 853–860.

Nykänen, V., Niiranen, T., Molnár, F., Lahti, I., Korhonen, K., Cook, N., Skyttä, P., 2017. Optimizing a knowledge-driven prospectivity model for gold deposits within Peräpohja Belt, Northern Finland. Natural Resources Research 26, 571–584.

Orlando, A., 2023. Prodigy Gold: Applying Mineral Potential Modelling of the Granites Tanami Orogen in Australia. Special Features. Mining.com.au, 12 May 2023. Available online at: https://mining.com.au/prodigy-gold-applying-mineral-potential-modelling-of-the-granites-tanami-orogen-in-australia/ (last accessed on 22 September 2024).

Parsa, M., 2021. A data augmentation approach to XGboost-based mineral potential mapping: an example of carbonate-hosted ZnPb mineral systems of Western Iran. J. Geochem. Explor. 228, 106811.

Parsa, M., Maghsoudi, A., Yousefi, M., 2018. A receiver operating characteristics-based geochemical data fusion technique for targeting undiscovered mineral deposits. Nat. Resour. Res. 27, 15–28.

Parsa, M., Carranza, E.J.M., Ahmadi, B., 2022. Deep GMDH neural networks for predictive mapping of mineral prospectivity in terrains hosting few but large mineral deposits. Natural Resources Research 31, 37–50.

Prodigy Gold NL, 2023. Mineral potential modelling of gold systems in the Tanami: a multi-technique approach to support the next discovery in the NT. In: AGES Conference Presentation, Alice Springs, Northern Territory, 18–19 April 2023, 24 p.

Prodigy Gold NL, 2024. Presentation–Exploration Update, February 2024. Announcement to the Australian Securities Exchange (ASX) dated 13 February 2024. 18 p.

Rezaei, J., 2015. Best-worst multi-criteria decision-making method. Omega 53, 49–57.

Riahi, S., Bahroudi, A., Abedi, M., Aslani, S., 2023a. A comparative analysis of multi-index overlay and fuzzy ordered weighted averaging methods for porphyry Cu prospectivity mapping using remote sensing data: the case study of Chahargonbad area, SE of Iran. Geocarto International 38, 2159068.

Riahi, S., Fathianpour, N., Tabatabaei, S.H., 2023b. Improving the accuracy of detecting and ranking favorable porphyry copper prospects in the east of Sarcheshmeh copper mine region using a two-step sequential Fuzzy-Fuzzy TOPSIS integration approach. Journal of Asian Earth Sciences: X 10, 100166.

Roshanravan, B., Agajani, H., Yousefi, M., Kreuzer, O., 2018. Generation of a geochemical model to prospect podiform chromite deposits in North of Iran. Generation of a geochemical model to prospect podiform chromite deposits in North of Iran. In: 80th EAGE Conference and Exhibition 2018, 2018. European Association of Geoscientists & Engineers, pp. 1–5. No. 1.

Roshanravan, B., Aghajani, H., Yousefi, M., Kreuzer, O.P., 2019. An improved prediction-area plot for prospectivity analysis of mineral deposits. Natural Resources Research 28, 1089–1105.

Roshanravan, B., Kreuzer, O.P., Bruce, M., Davis, J., Briggs, M., 2020. Modelling gold potential in the Granites-Tanami Orogen, NT, Australia: a comparative study using continuous and data-driven techniques. Ore Geol. Rev. 125, 103661.

Roshanravan, B., Kreuzer, O.P., Mohammadi, S., Bruce, M., Davis, J., Briggs, M., 2021. Cuckoo optimization algorithm for support vector regression potential analysis: an example from the Granites-Tanami Orogen, Australia. Journal of Geochemical Exploration 230, 106858.

Roshanravan, B., Kreuzer, O., Buckingham, A., Keys, E., 2023a. On data quality in mineral potential modelling: a case study using random forest and fractal techniques. In: In 84th EAGE Annual Conference & Exhibition, 2023. European Association of Geoscientists & Engineers, pp. 1–5. No. 1.

Roshanravan, B., Kreuzer, O.P., Buckingham, A., Keykhay-Hosseinpoor, M., Keys, E., 2023b. Mineral potential modelling of orogenic gold systems in the Granites-Tanami Orogen, Northern Territory, Australia: a multi-technique approach. Ore Geol. Rev. 152, 105224.

Saaty, T.L., 1980. The analytic hierarchy process (AHP). J. Oper. Res. Soc. 41, 1073–1076.

Stević, Ž., Pamučar, D., Kazimieras Zavadskas, E., Ćirović, G., Prentkovskis, O., 2017. The selection of wagons for the internal transport of a logistics company: a novel approach based on rough BWM and rough SAW methods. Symmetry 9, 264.

Stević, Ž., Pamučar, D., Puška, A., Chatterjee, P., 2020. Sustainable supplier selection in healthcare industries using a new MCDM method: measurement of alternatives and ranking according to COmpromise solution (MARCOS). Comput. Ind. Eng. 140, 106231.

Sun, T., Chen, F., Zhong, L., Liu, W., Wang, Y., 2019. GIS-based mineral prospectivity mapping using machine learning methods: a case study from Tongling ore district, eastern China. Ore Geol. Rev. 109, 26–49.

Vearncombe, J., Zelic, M., 2015. Structural paradigms for gold: do they help us find and mine? Appl. Earth Sci. 124 (1), 2–19.

Wyborn, L.A.I., Heinrich, C.A., Jaques, A.L., 1994. Australian Proterozoic mineral systems: essential ingredients and mappable criteria. AusIMM Publication Series 5 (94), 109–115.

Yousefi, M., Kreuzer, O.P., Nykänen, V., Hronsky, J.M., 2019. Exploration information systems–a proposal for the future use of GIS in mineral exploration targeting. Ore Geol. Rev. 111, 103005.

Zeng, S., Ye, A., Su, W., Chen, M., Llopis-Albert, C., 2024. Site evaluation of subsea tunnels with sightseeing function based on dynamic complex MARCOS method. Technol. Forecast. Soc. Chang. 199, 123041.

Zou, K.H., O'Malley, A.J., Mauri, L., 2007. Receiver-operating characteristic analysis for evaluating diagnostic tests and predictive models. Circulation 115, 654–657.

Zuo, R., Xiong, Y., Wang, Z., Wang, J., Kreuzer, O.P., 2023. A new generation of artificial intelligence algorithms for mineral prospectivity mapping. Natural Resources Research 32, 1859–1869.